Chapter 4

Electrodeposited Phosphorous Doped Graphitic Carbon Nitride for Electrocatalytic Oxidation of Tryptophan.

4.1. Introduction.

L-tryptophan, often known as TRP, is one of the eight essential amino acids that are considered to be important for human growth.[1–4] The importance of TRP stems from its involvement in the biosynthesis of a number of essential biomolecules/enzymes, including serotonin, adrenaline, dopamine, melatonin, vitamin B_3, quinolinic acid, kynurenic acid, tryptamine, melanin etc.[5] TRP is also crucial for production and maintenance of body proteins and muscles. Furthermore, it plays a vital role in maintaining a positive nitrogen ion balance,[6] and ensuring the metabolic homeostasis of our brains. To maintain nitrogen ion equilibrium, it is necessary for an adult to consume a daily amount of 4 mg of TRP per kg of body weight.[7] Because the body is unable to produce the essential amino acids on its own, they must be obtained through diet or through the nutritional supplements. TRP is widely utilised in the health supplement industry for a variety of benefits, including controlling the state of mind and the improvement of sleep.[8,9] Cheese, peanuts, chicken, fish, milk, beans, oats, dark chocolate bars, eggs, bananas, apples, dried prunes, and dark chocolate are some of the foods that contain TRP.[10] However, it is important to maintain the optimum level of TRP in human body. Both the overabundance of TRP as well deficiency can be harmful to a person's health and lead to clinical symptoms and diseases. Inadequate levels of TRP have been linked to symptoms such as tiredness, hair loss, and skin lesions, pellagra, tremors, hyperactivity, myoclonus, and Parkinson's disease.[11] Elevated levels of TRP, on the other hand, have been linked to adverse effects such as nausea, drowsiness, dizziness, lack of appetite, kidney, and liver problem.[12] However, a number of studies have found that an enhanced TRP metabolism can be detrimental to the central nervous system and may contribute to the acceleration of the processes that lead to ageing and dementia.[13] In addition, consuming an excessive amount of TRP can lead to the development of

eosinophilia-myalgia syndrome, a significant medical illness that is primarily characterised by intense muscle pain and weakness.[14] An atypical metabolism of TRP causes the production of a poisonous chemical in the brain, which can lead to symptoms of schizophrenia such as hallucinations and delusions.[15] As a result, it is extremely important to develop a method that is precise, quick, and economical for determining the TRP levels in dietary product, commercial nutritional supplements as well as clinical samples.

As of the present, a multitude of analytical methods have been developed to detect and quantify TRP in a vast array of real-world samples. These methods include chromatographic techniques (e.g., HPLC,[16] GC,[17] TLC,[18] or ion exchange[19]), spectrophotometric assays[20], fluorescence,[21] and capillary electrophoresis.[22] Every method possesses its own set of benefits and drawbacks. Most spectrophotometric and fluorescence methods have poor TRP selectivity, and chromatographic methods necessitate lengthy sample pre-treatments and lengthy analysis times. These methods also had other drawbacks, such as costly instrumentational set-up, complex analytical processes, and use of toxic and expensive solvents. The last decade has seen an upsurge of electroanalytical methods employed for the detection of bioactive compounds, food additives, and environmental contaminants.[22] Probably because to its unparalleled benefits, such as great sensitivity, low cost, miniaturized set-up for on-site detection ability/portability, low sample requirements and selective redox signature. More importantly, indolyl chemical structure of TRP offers significant electrochemical activity that makes its electrochemical detection easier.[23] However, the detection of TRP on bare electrodes is challenging due to the high overpotential caused by the lethargic kinetics of the electrode. Surface modified electrodes capable of electrocatalyzing TRP redox process can be a potential solution for achieving ultra-sensitive and selective

voltammetric TRP sensing. To date, numerous well-conceived heterostructures have been suggested as viable materials for the modification of electrochemical sensors. The exceptional physico-chemical traits of two-dimensional (2D) nanomaterials is widely recognized.[22] Graphitic carbon nitride (gCN), a well-known 2D polymeric material, has recently attracted a lot of attention due to its the distinctive properties, particularly its graphene-like planar structure that is made up of sp^2-linked carbon and nitrogen.[22] Apart from its remarkable physicochemical stability, gCN offers additional advantages such as its inexpensive and straightforward production and its effortless functionalization.[24] The π-conjugated structure of the compound enables it to engage in π-π interactions with a diverse array of biological substances. In addition, gCN's N-rich triazine structural units, which include pyridinic and graphitic N species, provide it with a wide variety of electron donor sites for use in chemical and biological reactions.[25] However, the actual implementation of gCN is limited due to its inherent low electrical conductivity, hindered charge transfer, and insufficient solubility in solvents.[26] These limitations impose restrictions on the use of gCN in electrochemical systems. In order to adequately tackle these limitations, it was determined that the most suitable strategy would entail customising gCN by including heteroatoms via doping or surface impregnation.[27]

In general, the addition of heteroatoms/non-metals such as Boron (B),[28] Carbon (C),[29] Nitrogen (N),[30] Oxygen (O),[31] Phosphorus (P),[32] Fluorine (F),[33] Sulphur (S),[34] Selenium (Se),[35] to the gCN framework is an effective method to enhance the textural, optical, and electronic properties by increasing reactive sites and charge transfer mobility, among other factors. Additionally, the introduction of a heteroatom dopant is known to reduce its bandgap energy (Eg) via formation of a fermi level. The P-atom, which has a lesser electronegativity compared to the N atom, has a superior ability to donate electrons. By introducing a P-dopant into the structural framework of gCN, the delocalized-conjugated

system is enhanced, resulting in increased conductivity and electron transfer capabilities. Several articles have been published in recent years on the use of phosphorous doped gCN (P-gCN) catalyst in various applications, including hydrogen production, oxygen reduction reaction (ORR), photocatalytic activity, photocatalytic degradation, fluorescence probe, and electrochemiluminescence (ECL) reaction. Nevertheless, the use of P-doped gCN as a recognition element for electrochemical sensing has yet to be explored. To our knowledge, only a single publication reports the use of P-doped gCN for quercetin sensing, where the suspension was drop-coated on the electrode surface.[31] Therefore, this report focuses on synthesizing and electrodeposition P-doped gCN as a recognition element for TRP sensing. Furthermore, a thorough investigation was conducted to examine the impact of drop-coating and electrodeposition on the structure and electrochemical performance of the surface-modified electrode. The subsequent sections present a comprehensive discussion on the synthesis of P-doped gCN, electrodeposition protocols, and their optimization, comparative electrochemical analysis, and electroanalysis of TRP in a range of real samples, including food products, nutritional supplements, and human urine as a clinical sample.

4.2. Experimental:

4.2.1 Materials

Tryptophan, melamine, red phosphorous, potassium ferricyanide, potassium chloride, ascorbic acid uric acid, dopamine, hypo-xanthine, sodium dihydrogen phosphate, ortho-phosphoric acid, and disodium hydrogen phosphate were acquired from Alfa Aesar. The compounds were used in their original state without any further purification. A phosphate buffer solution with a concentration of 0.1 M was made following the procedure outlined by Christian and Purdy. The stock solution and test aliquots were prepared using deionized water acquired from a Milli-Q ultrapure water purifier.

4.2.2 Material Preparation

4.2.2.1 Synthesis of gCN

Melamine was used to produce graphitic carbon nitride (gCN) via pyrolysis method. Briefly, 10 g of melamine in an alumina crucible was heated in a muffle furnace. The furnace was heated up to 600 ℃ gradually using a ramp rate of 6 ℃/min. The furnace was maintained at 600 ℃ for 6 hours. Once the furnace reached the ambient temperature, the crucible was taken out to collect bulk gCN, a powder with a pale yellow tint. The resultant material was fine ground with a mortar and pestle and used for further characterization.

4.2.2.2 Synthesis of P-doped gCN

The P-gCN-x was produced by utilizing melamine and red phosphorus as the fundamental precursor. Specifically, 10 grams of melamine and different weight percentages (wt %) of Red P (x = 02,05, and 10) were dispersed in a 1:1 mixture of 10 mL of DI water and ethanol. To have effective mixing of the material, the suspension was stirred on a magnetic stirrer at 1000 rpm for 30 min. Afterwards, the solvent was subjected to complete evaporation. The resulting white powder was placed into a alumina crucible, and subjected to a heat treatment at a temperature of 600 ◦C for a duration of 6 hours, with an increasing ramp rate of 6 ◦C per minute. The obtained pale yellow powders were designated as P-gCN-02, P-gCN-05, and P-gCN-10, respectively.

4.2.3 Characterization details

The crystallographic data of the synthesized material was obtained using the X-ray Diffractometer (Rigaku miniflex 600, Japan), which employed a Cu-Kα radiation source. The surface functions of P-doped gCN were examined using Fourier-transform infrared (FT-IR) spectroscopy. The analysis was performed using the Thermo ScientificTM

Nicolet iD7 spectrometer, with a resolution of 4 cm^{-1}, within the wavenumber range of 550 – 4000 cm^{-1}. The ZEISS EVO scanning electron microscope was employed to get surface and morphological data. The material and modified electrode surfaces were subjected to elemental analysis using a K-Alpha X-ray photon spectrophotometer produced by Thermo Fisher Scientific. The device was fitted with a micro-focused X-ray source that employed monochromatic Al Kα radiation, operating within an energy range of 100-4000 eV. The NTEGRA Prima scanning probe microscope, made by NT-MDT Service & Logistics Ltd., was chosen for surface investigation utilizing atomic force microscopy.

4.2.4 Electrochemical measurements

The voltammetric analyzer designed by PalmSens3 was utilized in order to carry out the electrochemical measurements. The optimization study utilized a three-electrode setup consisting of Ag/AgCl (3M KCl) as a reference electrode, a counter electrode made of platinum wire, and glassy carbon electrode (GCE) as working electrode.

4.2.4.1 Electrodeposition of p-doped gCN Composite

The glassy carbon electrode (GCE) underwent mechanical polishing using an alumina powder slurry consisting of 0.05 μm, 0.3 μm, and 1 μm on a micro cloth pad, prior to electrodeposition. Subsequently, the polished electrode was thoroughly rinsed using DI water. In order to do the electrodeposition of P-doped gCN, 10 mg of the produced material was mixed with 10 mL of deionized water (DI) utilizing ultrasonic agitation in a bath sonicator for a duration of 2 hours. The aliquot utilized for electrodeposition was created by mixing 1 mL of the produced P-doped gCN suspension with 1 mL of a PB-7.4 buffer solution in an electrochemical cell.

Cyclic voltammetry (CV) was employed for carrying out the electrodeposition of the material. To do so, the voltage was scanned from -1.0 V to +1.6 V at a scan rate of 100 mVs^{-1}. The optimal number of scans (n) for electrodeposition was determined by systematically adjusting 'n' within the range of 5 to 25. After completing the required scans, the GCE was washed with deionized water and dried at room temperature. From this point forward, the term "P-gCN-X | GCE" has been used to denote the electrodeposited electrode.

4.2.4.2 Electroanalytical technique and sample preparation

To establish the optimized number of electrodeposition cycles, the electrochemical performance of the modified electrodes with variable “n” was recorded. A comparative evaluation was conducted by measuring the square wave voltammetry (SWV) peak current of a solution containing a 1:1 ratio of 1 mM $K_3[Fe(CN)_6]$ and 1 M KCl recorded using electrodes modified using different number of electrodeposition scans. The tests were done within a voltage range from -0.2 V to +0.6 V with a step size of 6 mV. The amplitude and frequency values were 25 mV and 10.0 Hz, respectively. After every SWV scan, the sensor was rinsed with DI water.

The electrodeposited surface's potential for voltammetric sensing applications was evaluated with TRP as the analyte of choice. For qualitative and quantitative electroanalytical investigations, the required amount of TRP was dissolved in deionized water (DI) to make a 1 mM stock solution. Dilution method was used for preparing TRP solutions of different concentrations. For every sample, the amount of PB-7.4 was kept fixed as 1 mL. The remaining 1 mL was composed of DI and the required volume of TRP stock solution. The electrochemical signals were recorded using both CV and SWV in a potential range of 0 to 1 V. The experimental parameters were: a step size of 6 mV, amplitude and frequency values were 25 mV and 10.0 Hz, respectively. After every SWV

scan, the sensor was rinsed with DI followed by surface stabilization by recording five SWVs in a buffer solution.

Real Sample Preparation:

Almond as real sample

One almond, amounting to 1.082 g, was crushed with a mortar and pestle. To produce the appropriate paste consistency, 2 mL of DI water was added to the mortar pestle. The paste was collected as stock and utilized to create a test sample. One sample was generated by combining 1 mL of the resulting paste with 1 mL of PB-7.4.

Carrot as real sample

Carrots were chopped into tiny pieces. A little piece weighing 2g was crushed using a mortar pestle. It was then combined with 2 mL of DI water to form a paste. 1 mL of the prepared paste was then extracted and poured to a glass cell containing 1 mL of PB-7.4.

Chickpea as real sample

One soaked chickpea weighing 0.91g was mashed with a mortar and pestle. 2 mL of PB-7.4 was added to the crushed chickpea to create a suspension. A test sample of 2 mL was extracted from the prepared solution.

Egg white as real sample

1 mL of egg white was mixed with 1 mL of PB-7.4. This was taken as the test sample.

Kidney beans as real sample

Two pieces of soaked kidney beans weighed 3.2g were taken and mashed using a mortar and pestle. To form a suspension, 2 mL of DI was added to the mashed kidney beans. 1 mL of the suspension was collected and mixed with 1 mL of PB-7.4 to serve as the test sample.

Oats as real sample

1g of oats were crushed into powder using a mortar and pestle. To create a suspension, 5 mL of DI was added to the powder. 1 mL of the colloidal suspension was then pipetted out and mixed with 1 mL of PB-7.4 and used as a test sample.

Pista as real sample

1 Pista was crushed into powder. 5mg of the powder was taken and suspended into 1:1 (by volume) of DI water and PB-7.4 to make a test sample of 2mL.

Pumpkin as real sample

A chopped piece of pumpkin weighing 2g was mashed with a mortar and pestle. It was mixed with 2 mL of DI water to form a dilute paste. 1 mL of the liquid was then mixed with 1 mL of PB-7.4 and used for analysis.

Turmeric powder as real sample

The test solution of turmeric was prepared by suspending 1g of turmeric powder to 2mL mixture of DI water and PB-7.4 (1:1 by volume). The prepared suspension was thoroughly stirred for 1 hr. The prepared sample was filtered and supernatant was used for analysis.

Urine as real sample

1 mL of urine of a healthy volunteer (Male, 24 Y) was filtered employing a syringe filter and was mixed with 1 mL of PB-7.4. The diluted solution was used directly for analysis

L-Tryptophan capsule as real sample.

As per the tabulated contents, each Oxin Nutrition L-Tryptophan capsule contains 500 mg of L-Tryptophan. The capsule was opened, and 1 mg of capsule powder was taken and combined with 4.89 mL DI water which resulted in a stock solution of 1 mM stock solution. The stock solution was diluted to make desired solution of 10 µM, 20 µM, 30 µM, respectively.

Human blood serum as real sample.

Blood serum sample of a healthy 24-year-old male volunteer was collected from the nearby pathology lab. 1 mL of blood serum was filtered through a syringe filter and added to 1 mL of water. 1 mL of the diluted solution was then mixed with 1 mL of PB-7.4. This was used as the testing sample.

4.3. Results and Discussion

4.3.1 Material Characterization: Examining the gCN and P-doped gCN composites

Several characterisation techniques were used to examine the topographical, chemical, and physical characteristics of the as synthesized gCN and different P-doped gCN composites. The powder X-ray diffraction (PXRD) patterns of the synthesized gCN and P-doped gCN are presented in **Figure 4.1(a)**. The X-ray diffractogram of the gCN showed a distinct peak at 27.5°, indicating the presence of the (002) plane, which is a unique feature of the graphite-like structure with stacked layers of conjugated aromatic groups. A tiny diffraction peak at 13.1° indicates the arrangement of aromatic structures within the same plane.[36,37] The d-spacing between the gCN layers was around 0.33 nm, calculated using the theta values of the most intense peak. The investigation revealed a notable shift in the position of the (002) plane showcasing a 2θ value of 27.71°, 27.83°, and 27.70° for P-gCN-02, P-gCN-05 and P-gCN-10, respectively. These values deviated by more than 0.15° from the 2θ value of 27.55° observed for gCN. The shift indicates the successful doping of P into gCN lattice and the observed shift was in accordance to the previously reported values.[38–40] The deviation of peak position and gradual decrease in intensity seen with increasing phosphorus content were caused by infiltration of P-atoms in the gCN matrix.[41] Nevertheless, the PXRD patterns exhibit peaks corresponding to both the planes of gCN indicating considerably retained structure even after P-atom doping.[42]

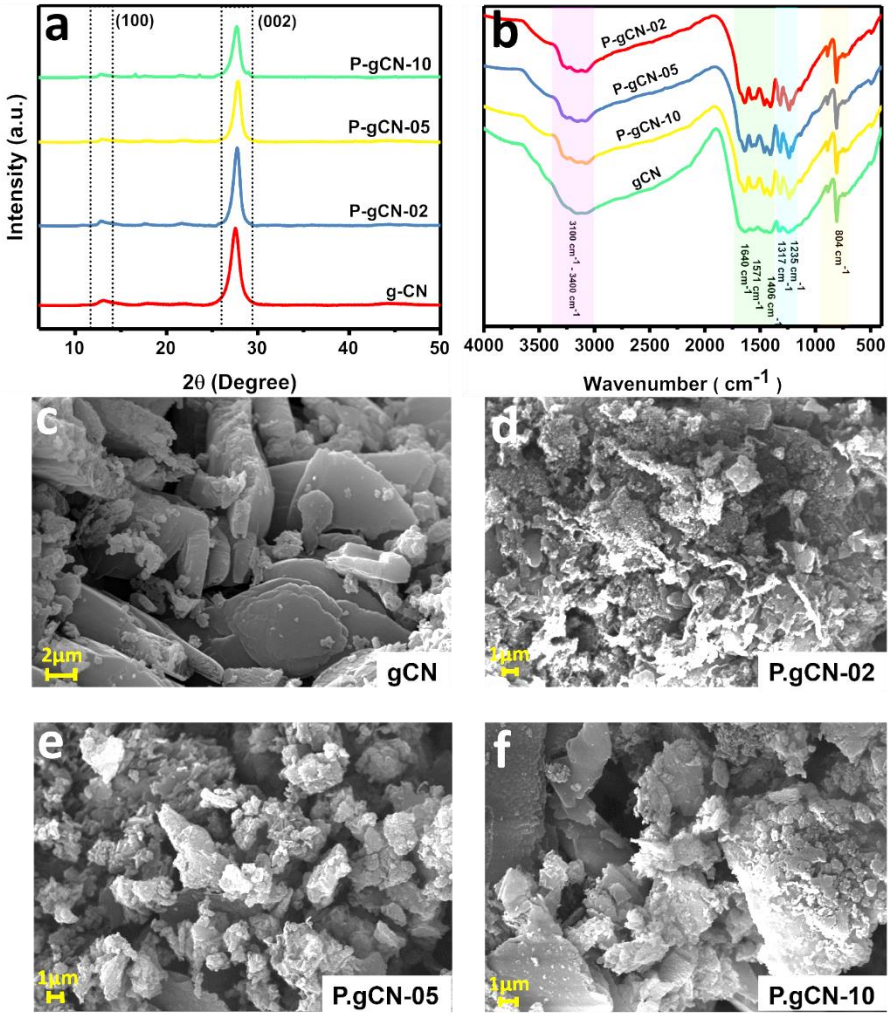

Figure 4.1: (a) XRD comparison of as synthesized gCN and all different P doped gCN composite. (b) FT-IR comparison of as synthesized gCN and all different P doped gCN. HR-SEM image of (c) gCN, (d) P-gCN-02, (e) P-gCN-05, and (f) P-gCN-10.

In order to gain useful insights on the chemical bonds and functional groups that are present in the material, Fourier-transform infrared (FT-IR) spectroscopy was next utilized. **Figure 4.1(b)** illustrates the FT-IR spectra of gCN and P-doped gCN composites. The spectra display a wide peak between 3100 - 3400 cm^{-1}, indicating the existence of -NH and -OH groups on the surface of the gCN. The -NH group signifies the unbound amino groups on the non-polymerized triazine rings. The -OH group represents oxygen-containing surface impurities such as carbonates and water molecules that are adsorbed on the gCN surface. The different vibrations of the C-N bonds that make up the polymeric arrangement of triazine rings are represented by many peaks between

1100 and 1600 cm^{-1}. The triazine units inside the gCN framework display a unique out-of-plane bending/breathing vibration mode, shown by the prominent peak at 804 cm^{-1}, indicating successful formation of gCN.[43–45] The P-gCN doped materials exhibited a similar spectrum, indicating that P-doping does not disrupt the basic gCN framework.

To investigate the effect of P doping on particle sizes, the scanning electron microscopic measurements of gCN and P-doped gCN were carried out. The HR-SEM images of gCN showcased smooth microscale plate-like structures (**Figure 4.1(c)**). Whereas much smaller particle sizes were observed for different P doped gCN (**Figure 4.1(d-f))**. The HR-SEM thus validated the inferences made from XRD and FTIR analysis and confirmed that P-doping resulted in altered crystal size and topography.

X-ray photoelectron spectroscopy was subsequently employed to acquire additional insights regarding the chemical composition of the elements present in the synthesized materials. The XPS survey spectra of gCN and PgCN-05 confirmed the presence of carbon and nitrogen (N) components **(Figure 4.2(a))**. In addition, the P-doping in gCN was confirmed from the presence of two extra peaks between 120 and 200 eV, corresponding to P 2p and P 2s which were not observed in bulk gCN. The peak at 133.7 eV in P 2p spectrum **(Figure 4.2(b))** is associated with a P−N coordination (P−C bonding would be about 1-2 eV lower)[46] further confirming the penetration of P into the gCN lattice.[41,47,48] The deconvoluted high-resolution C 1s and N 1s XPS spectra of gCN and P-gCN-05 are shown in **Figure 4.2(c,d) and 4.2(e,f)**. The high resolution, C 1s spectrum of both the materials exhibited five peaks at the following energies: 284.3, 285.1, 287.8 eV, 288.4, and 293.4. The adventitious reference carbon on the surface is usually thought to be the source of the C 1s peak centred at 284.3 eV. The sp^2 C-C bonds in graphitic carbon nitride is responsible for the peak that originated at 285.1eV.[49,50] The C 1s signal at 287.8 eV is due to bonds between sp^2 C atoms and N (N=C-N) in triazine ring. The

peak at 288.3 eV is attributed to sp^2 C atoms in the aromatic ring connected to the primary and secondary amines (carbon atoms coupled with three N neighbours, N=C-(N)-NH, N=C-(N)-NH_2).[51–54] While the aromatic shake-up satellite peaks originating from the π cloud of polymeric triazine structures of gCN are matched to the C 1s peak located at 293.4eV.[55–57] Compared to gCN, the peaks were found to be slightly shifted towards higher binding energy in the C 1s spectra of P-gCN-05, presumably indicating P-doping (n-type doping). The N 1s spectra of both the materials showed four signals from distinct nitrogen environments in the triazine structural unit, with binding energies of 398.3 eV, 399.5 eV, 400.7 eV, and 403.8 eV.

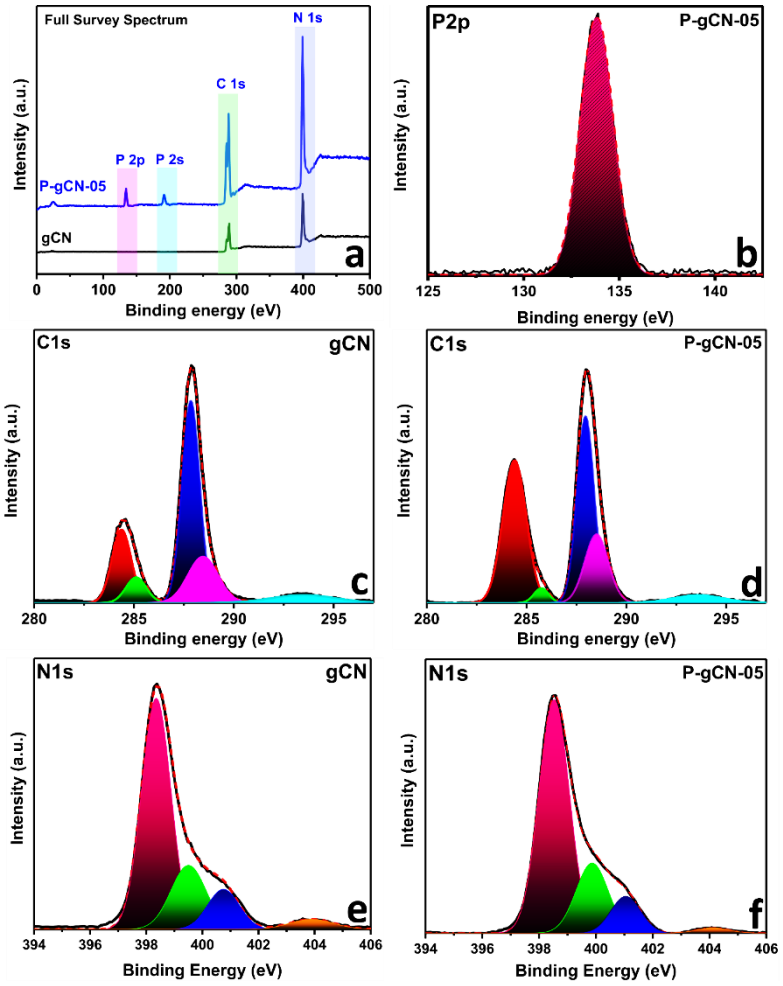

Figure 4.2: (a) XPS full survey comparison of as synthesized gCN and P-gCN-05 (b) High resolution deconvoluted P 2p spectra of P-gCN-05 (c) High resolution deconvoluted C 1s spectra for gCN. (d) High resolution deconvoluted C 1s spectra compare for P-gCN-05. (e) High resolution deconvoluted N 1s spectra for gCN. (f) High resolution deconvoluted N 1s spectra compare for P-gCN-05.

The peak at 398.3 eV is associated with nitrogen atoms that are sp^2-bonded to two carbon atoms (C=N-C). The peak at 399.5 eV represents nitrogen atoms bound to three sp^2 carbon atoms in the C–N network [N-$(C)_3$]. The peak at 400.7 is attributed to N-H groups located at the open ends of the gCN network. Quaternary nitrogen, which are oxidized nitrogen species, are detected in the N 1s spectra with a binding energy of 403.8 eV.[53,58–60] Once again, the N 1s spectra of P-gCN-05 showed a little shift in all of the binding energy values arising due to P-N interaction. From the detailed spectrometry and microscopic characterization, the successful P doping in gCN was confirmed. Therefore, the electrochemical characteristics of the synthesised materials were next investigated.

4.3.2 P-doped gCN electrodeposition and understanding the fundamental process:

Several publications have been published detailing the utilization of gCN modified surfaces for creating electrochemical sensors. Yet, in the earlier articles, it was immobilised onto the electrode surface by drop-casting. Non-uniform particle dispersion, human error-related spreading concerns, and uncontrolled loading are challenges with drop-casting.[61] To tackle drop-casting problems, our study introduces an unusual gCN and P-doped gCN electrodeposition approach. In our previous publication, we have reported the electrodeposition of bulk gCN on the ITO coated glass substrate.[62] However, in this work electrodeposition of bulk gCN and P-doped gCN is targeted on a challenging glassy carbon electrode. The detailed electrodeposition protocol is given in experimental section. The cyclic voltammograms (CV) observed during electrodeposition of both the materials are presented in **Figure 4.3(a,b)**. The careful analysis of CV was carried out to understand the mechanism underlying the growth of surface layer. The CV of both the material exhibits two peaks; one around 1.0 V, caused by the electropolymerization of the triazine ring, and the other near 1.3 V, caused by the formation of radical cation.[62,63]

With an increase in the number of scans, the polymerization peak current was found to increase for both the samples.

However, the greater conductivity of P-doped gCN makes the enhancement more noticeable. Following that, the impact of surface modification on the electrochemical performance of the electrode was observed and analyzed. The comparative electrochemical response of 0.5 mM $K_3[Fe(CN)_6]$ in KCl recorded using bare GCE, gCN modified GCE (gCN | GCE), and different P doped gCN is shown in **Figure 4.3(c)**. For all the modifications 15 CV scans were run for electrodeposition. It is clear from the figure that surface modification using all the four samples led to an increase in peak current. However, P-gCN-05 | GCE demonstrated the greatest improvement, with a peak current that was roughly two times larger than that of the bare GCE. Consequently, in order to attain the optimal electrochemical response, the electrodeposition of P-gCN-05 | GCE was further optimized.

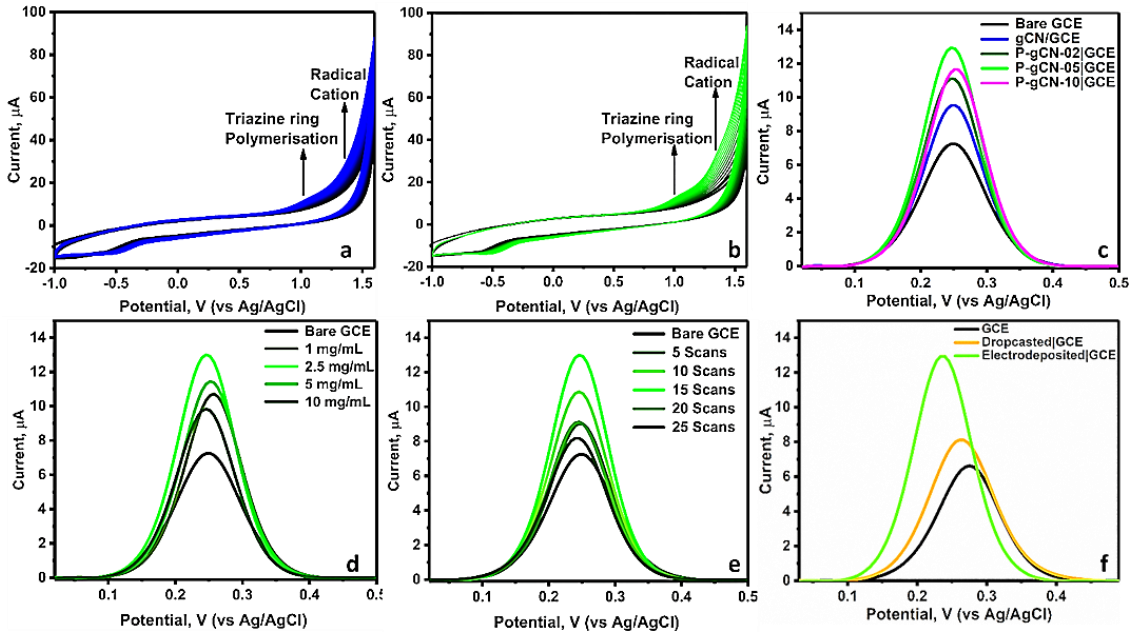

Figure 4.3: Cyclic voltammograms observed during electrodeposition of (a) gCN and (b) P-gCN-05. (c) Square wave voltammograms observed for 0.5 mM $K_3[Fe(CN)_6]$ in KCl using bare GCE, gCN | GCE, P-gCN-02 | GCE, P-gCN-05 | GCE and P-gCN-10 | GCE. Square wave voltammograms observed for 0.5 mM $K_3[Fe(CN)_6]$ in KCl using P-gCN-05 | GCE as a function of (d) different suspension concentrations of P-gCN-05, (e) Increasing numbers of electrodeposition cycles, (f) surface modification method i.e. drop casted P-gCN-05 | GCE, and electrodeposited P-gCN-05 | GCE.

4.3.2.1 Protocol Optimization

The benefits of modifying electrodes are proportional to the thickness of the electrodeposited surface. To obtain the required electrochemical performance, the thickness of the electrodeposited coating was optimized by modifying the electrodeposition parameters, such as the concentration of solution and the number of scans. This was accomplished by conducting the electrodeposition using a P-gCN-05 suspension at four different concentrations which are 1 mg/mL, 2.5 mg/mL, 5 mg/mL, and 10 mg/mL keeping the number of electrodeposition scans fixed at 15. The comparison was based on the SWV peak current of 0.5 mM $K_3[Fe(CN)_6]$. **Figure 4.3(d)** displays the comparative SWV responses. The electrode, modified with a 2.5 mg/mL suspension, had the highest peak current with more than two times increment compared to bare electrode. The electrode treated with 1 mg/mL has a lower material concentration on the surface, leading to a reduced current response compared to 2.5 mg/mL. Whereas, the peak current exhibited by electrodes modified with 5 and 10 mg/mL was lower than observed for 2.5 mg/mL. This could be because of electrodeposition of a thicker layer ascribed to use of denser suspension. As a result, we determined that 2.5 mg/mL was the optimal suspension concentration and investigated the number of deposition cycles required to achieve the best electrochemical performance. **Figure 4.3(e)** illustrates the relationship between the number of deposition cycles (n) and the resulting variations in the peak current. The peak current increased as the number of deposition scans increased up to n = 15. However, a decrease in the current was observed for n > 15, perhaps due to the deposition of thicker P-gCN-05 layer. A thicker layer acts as a physical barrier that hinders the flow of electrons from the working electrode to the analyte, thereby preventing electron transfer. Therefore, the best parameters for the surface modification procedure were found to be a suspension concentration of 2.5 mg/mL and 15

electrodeposition scans. All further experiments employing P-gCN-05 | GCE were modified using the same settings.

To outline the benefits of electrodeposition over drop casting, the electrochemical performance of bare, drop-casted, and electrofunctionalized P-gCN-05 | GCE were compared and are shown in **Figure 4.3(f)**. Compared to the drop-casting method, the electro-functionalization process displayed substantially larger peak currents. Furthermore, the electrodeposited sample exhibited a electrocatalytic property showcasing a potential shift of 0.10 V which was not observed with the drop-casted electrode. The electrocatalytic activity can be ascribed to the specific redox processes that lead to electropolymerization of P-gCN on GCE surface which doesn't take place in simple drop-casting. In addition, the electrodeposition offers a precise control of the layer thickness as a function of deposition cycles or suspension concentration leading to uniform surface modification. On the other hand, agglomeration, uneven loading of materials, human error, and insufficient interfacial contact are problems with drop casting because of which, a compromised electrochemical performance is achieved. Therefore, P-gCN-05 | GCE scaffold fabricated using electrodeposition was selected and thoroughly characterized to investigate its compositional, surface and topographical characteristics.

4.3.2.2 Surface Characterization

XPS was carried out to investigate the composition of the electrodeposited layer. **Figure 4.4(a)** shows the complete full survey region XPS spectra for P-gCN-05 | GCE. Carbon (C) and nitrogen (N) were verified to be present in the XPS complete survey spectra of P-gCN-5 | GCE. The two peaks between 120 and 200 eV correspond to P 2p and P 2s indicating the presence of P in the electrodeposited layer. The high-resolution deconvoluted C 1s XPS spectra **(Figure 4.4(b))** showcase three peaks at 284.7 eV, 285.8 eV, and 288.2 eV corresponding to the carbon-carbon coordination of the adventitious

carbon on the surface, the sp^2 C-C bond, and the sp^2 C atoms linked to the primary and secondary amines, respectively.[37,49,60,64] The C 1s spectra manifested the well retained gCN framework in the electrodeposited surface.

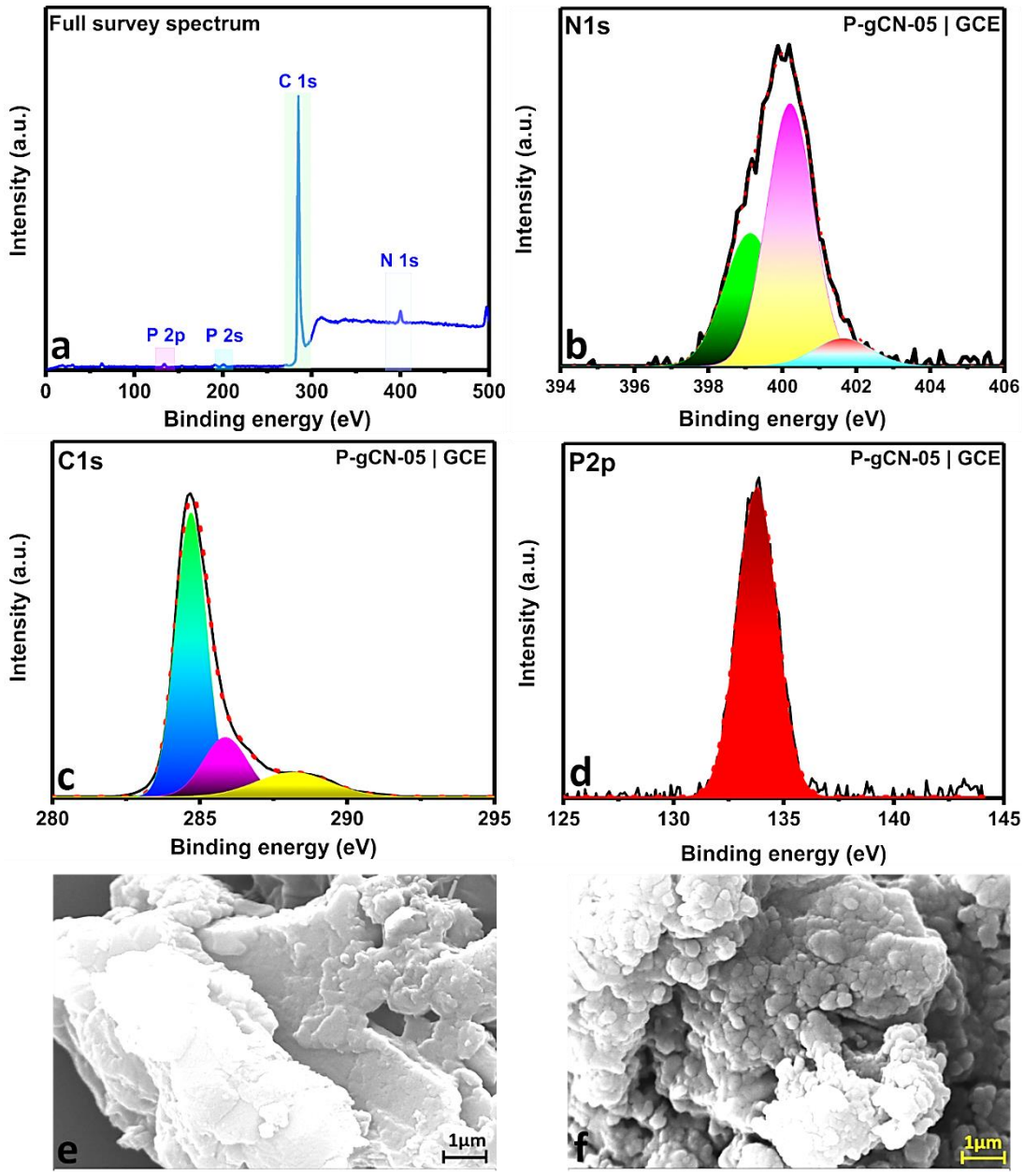

Figure 4.4: X-ray photoelectron spectra of (a) Full survey for P-gCN-05 | GCE (b) Deconvoluted spectra of C 1s (c) Deconvoluted spectra of N 1s, and (d) Deconvoluted spectra of P 2p for P-gCN-05 | GCE. HR-SEM image of (e) Electrodeposited gCN | GCE and (f) Electrodeposited P-gCN-05 | GCE.

The three different nitrogen environments of triazine structural unit of gCN was also confirmed from the N 1s spectra **(Figure 4.4(c))** demonstrating three signals with binding energies of 399.1 eV, 400.2 eV, and 401.6 eV, respectively. The peak located at 399.1

eV is associated with sp^2 hybridized nitrogen bonded to carbon (C−N=C) in triazine rings. Trigonally bonded N atoms to three sp^2 carbon atoms in the C–N network ($N\text{-}(C)_3$) may account for the peak at 400.2 eV. The peak at 401.6 eV can be attributed to the open end N-H groups present in the graphitic carbon nitride network.[65,66]

Furthermore, **Figure 4.4(d)** shows the high-resolution P 2p spectra at 133.7 eV, which corresponds to the P-N bond.[41,47,48] Therefore, the XPS analysis of electrodeposited surface confirmed the electrodeposition of P doped gCN on the electrode surface.

Next, the surface changes occurred due to electrodeposition was visualized using HR-SEM. **Figure 4.4(e,f)** shows HR-SEM images of the gCN | GCE and the P-gCN-05 | GCE. The microscopic images of both the electrodeposited gCN | GCE and P-gCN | GCE provided evidence of substantial changes in the surface of GCE. The electrodeposition of gCN resulted in the growth of smooth plate-like structures on the otherwise flat GCE surface. The P-gCN-05 | GCE also exhibited similar plate like base structures. However, in contrast to the smooth surface of gCN plates, the bulged out structures were observed on the surface of P-gCN. These 3D bulges were consistent in size and occurred all across the surface. Elemental mapping and EDX **(Figure 4.5)** verified the uniform distribution of C, N, and P on the electrodeposited surface.

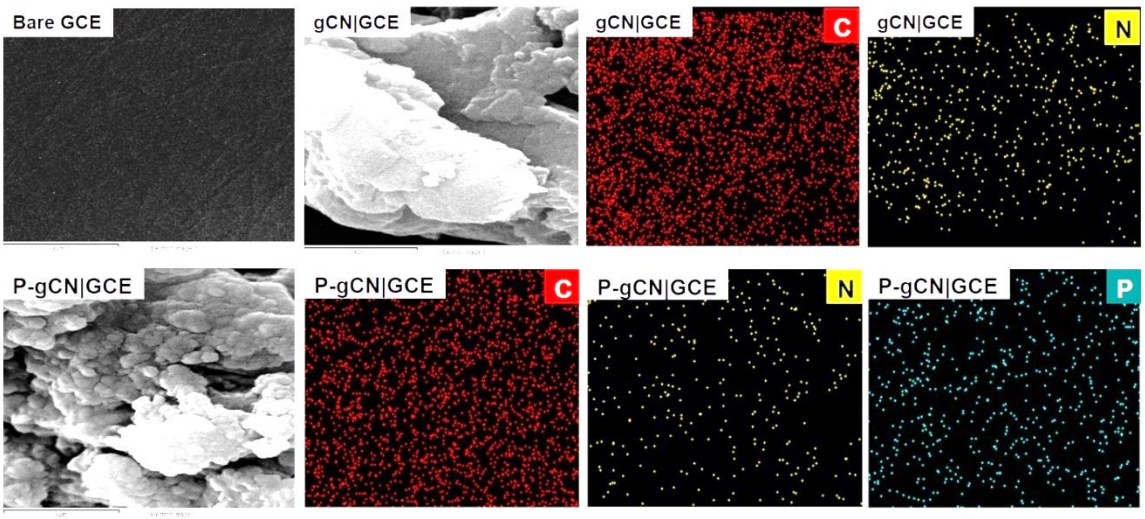

Figure 4.5: SEM Images of Bare GCE, gCN | GCE and P-gCN | GCE with corresponding elemental mapping of gCN | GCE and P-gCN-05 | GCE

The next step was to examine the changes in surface roughness and layer thickness using atomic force microscopy (AFM). According to the AFM peak profile presented in **Figure 4.6(a-d)**, the average peak height of the P-gCN-05 | GCE composite is 31.06 nm, which is much higher than the 14.02 nm peak height of the uncoated GCE. The difference in the peak heights indicated the electrodeposition of 16.61 nm thick layer on the GCE surface. In addition, the electrochemically tuned surface had a root mean square roughness that was found to increase from 3.20 nm to 3.73 nm after electrodeposition. The AFM analysis thus manifested the electrodeposition of surface layer that lead to increased surface roughness which can incentivise charge transfer on the modified electrode surface.

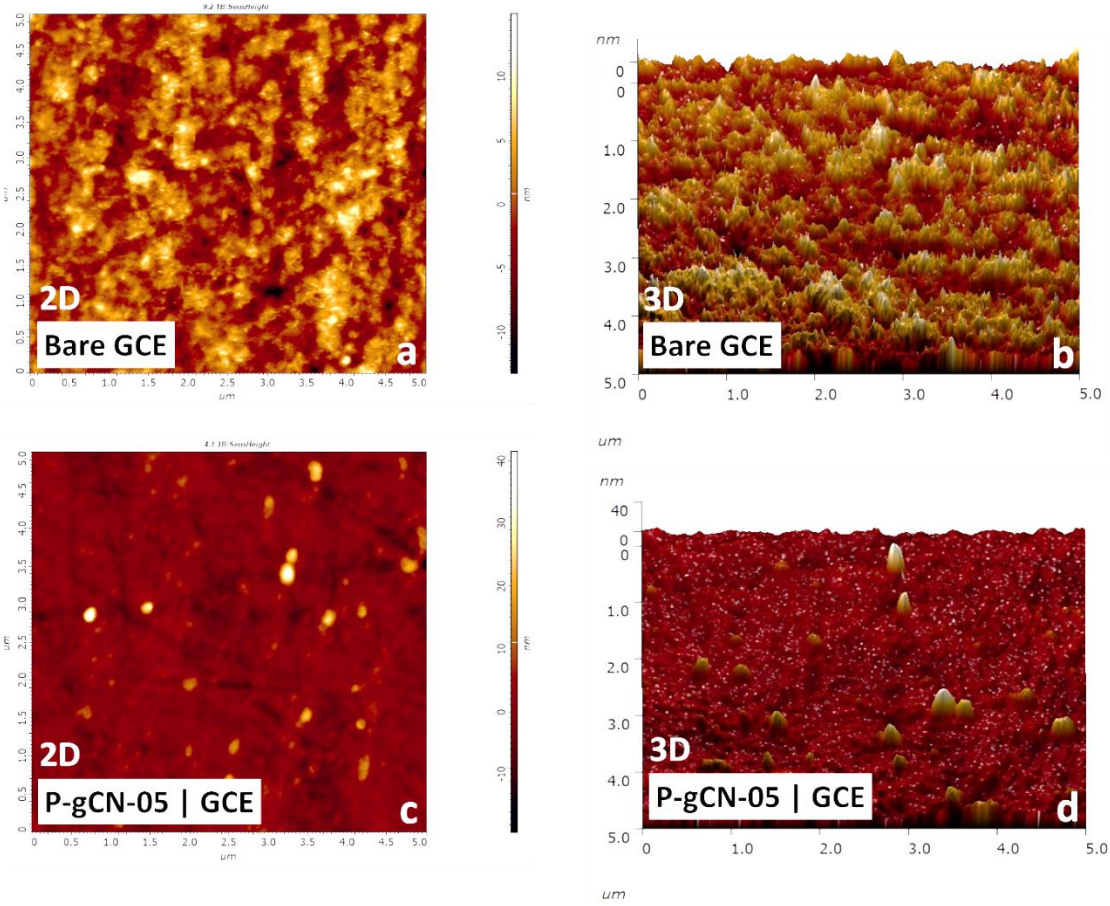

Figure 4.6: AFM profiles observed for the (a, b) Bare GCE and (b, d) P-gCN-05 | GCE.

The 3D bulge-out shape and increased roughness observed in HR-SEM and AFM analyses suggests that the electro-functionalized substrate has a larger number of electroactive sites, leading to an expected increase in the electrochemical surface area

and an improvement in electrochemical charge transfer. Consequently, an evaluation was conducted to determine the electroactive surface area of the electrode for both the modified P-gCN-05 | GCE and the bare GCE. To do so, we varied the scan rate from 5 to 100 mVs^{-1} while recording cyclic voltammograms of the Bare GCE and the P-gCN-05 | GCE in 1:1 by volume solution of 1 mM $K_3[Fe(CN)_6]$ and 1 M KCl. The voltammograms shown in **Figure 4.7 (a,b)** showcased two peaks corresponding to the reversible oxidation and reduction of the Fe^{2+}/Fe^{3+} couple. Scanning at higher rates did not produce any noticeable shift in potential, suggesting a reversible redox process mediated by diffusion. Using the Randles-Sevcik equation, we calculated the electrochemically active surface area of the bare and modified electrodes at a temperature of 25 °C.[67]

$$\mathbf{I_p = 2.69 \times 10^5\ n^{3/2}\ A\ D^{1/2}\ C\ \upsilon^{1/2}}$$

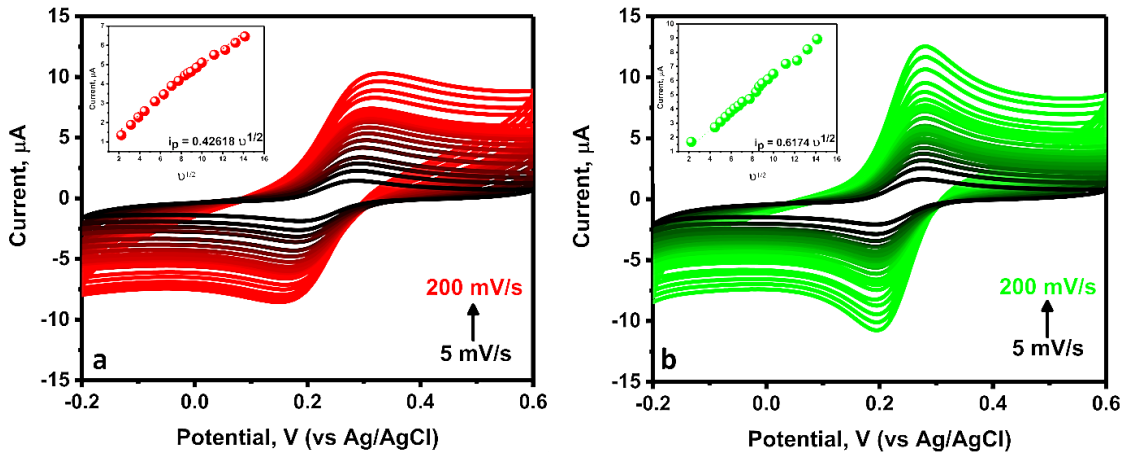

Figure 4.7: Cyclic Voltammograms recorded at different scan rates ranging from 5 mV/s to 200 mV/s using (a) Bare GCE, and (b) P-gCN-05 | GCE in 0.5 mM $K_3[Fe(CN)_6]$ solution.

Where, Ip stands for peak current (A), n for number of electrons transferred, A for electro-active area (cm^2), D for diffusion coefficient of $K_3[Fe(CN)_6]$ in KCl solution (7.4×10^{-6} cm^2s^{-1}), C for probe molecule concentration ($mol.cm^{-3}$), and υ for scan rate (Vs^{-1}). By analyzing the slope of the Ip vs. $\upsilon^{1/2}$ linear plots, we can determine that the bare electrode had an electroactive surface area of $0.0431cm^2$, whereas the modified electrode had an area of 0.0533 cm^2, making it 1.24 times larger than the bare GCE. After

electrodeposition, there was a noticeable rise in the current response, which may be attributed to the increased surface area, which can be translated into an increased number of feasible sites for interfacial electron transport. To test the surface functionalization's feasibility, the designed interface was employed to assess tryptophan (TRP), an essential amino acid which is critical for human growth.

4.3.3 Assessment of the modified electrode's analytical performance: Tryptophan sensing

Comprehensive surface and electrochemical comparisons reveal that P-gCN-05 | GCE has substantially enhanced electrochemical activity, which can result in enhanced electroanalytical sensitivity. Accordingly, P-gCN-05 | GCE's beneficial properties were then employed in the qualitative and quantitative assessment of Trp. **Figure 4.8(a,b)** represents the CV as well as SWV voltammograms recorded for 100 µM TRP by utilizing both bare and modified GCE. Both the voltammograms exhibited an TRP oxidation peak ~0.7 V. The comparative square wave voltammogram analysis revealed that the current response of the P-gCN-05 | GCE was around 7.5 times greater than that of the bare GCE. In addition, the P-gCN-05 | GCE displayed TRP electro-oxidation peak at 0.66 V compared to 0.76 V observed for bare GCE. This negative shift of ~0.10 V highlights the facilitated redox process and demonstrates the electro-catalytic activity of P-gCN towards TRP oxidation. The unique π-π interaction between the P-gCN and the aromatic ring of the TRP molecule, combined with H-bonding and the enhanced electroactive surface of the electrode can be ascribed to the notable increase in current and shift in potentials.[68] In order to perform a more comprehensive quantitative analysis, the calibration curve was constructed by observing the effects of different TRP concentrations on the associated current responses with both Bare GCE and P-gCN-05 | GCE. According to the findings, a linear rise in the peak current was found for both the bare and modified GCE electrodes

when the concentration of TRP increased. An illustration of the rise in peak current with the increasing TRP concentrations can be found in **Figure 4.8(c,d)**.

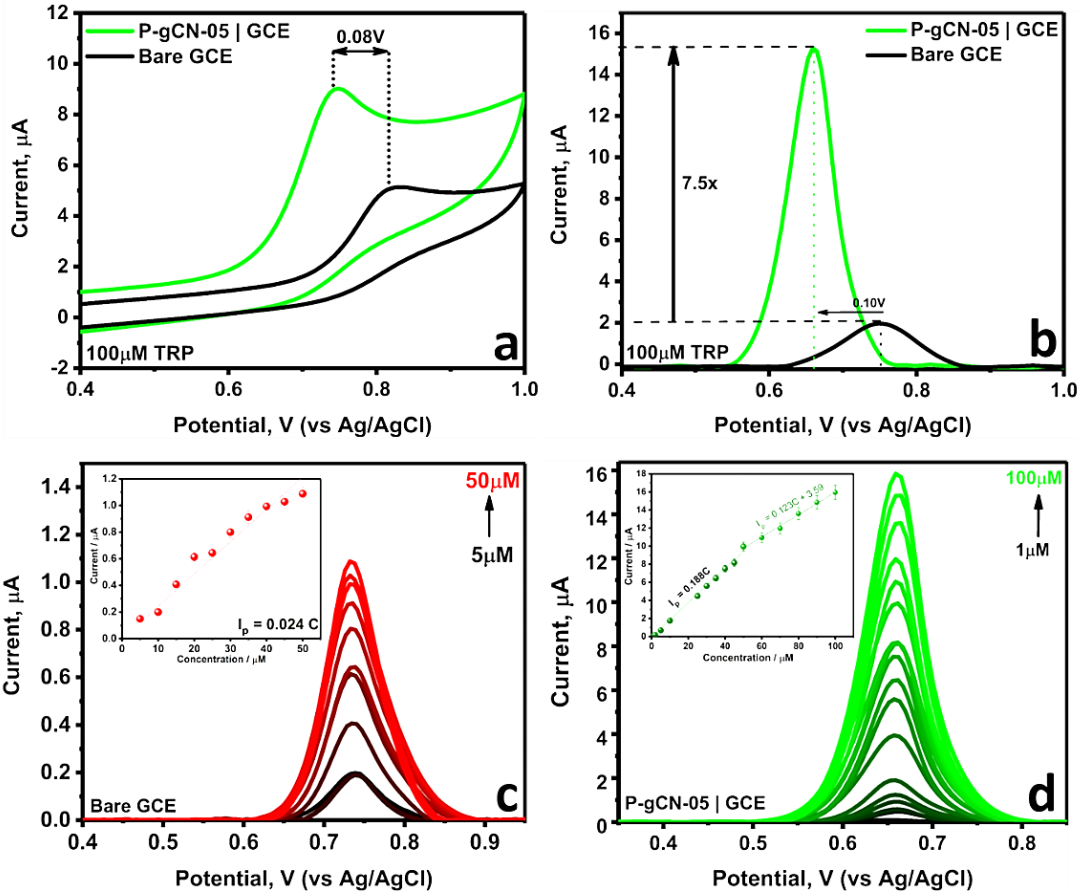

Figure 4.8: Comparative (a) Cyclic voltammograms (b) Square wave voltammograms recorded for 100μM TRP using Bare GCE and P-gCN-05 | GCE. Concentration study and corresponding correlation graph observed for (c) Bare GCE (d) P-gCN-05 | GCE.

The peak current (Ip) and the TRP concentration (C) were found to be correlated with the following linear regression equations.

$\boldsymbol{I_p}$ (μA) = 0.188 **C** [1-60 μM]; R^2 = 0.9978……..**:** P-gCN-05 | GCE

$\boldsymbol{I_p}$ (μA) = 0.123 **C** [60-100 μM] + 3.59; R^2 = 0.9944……..**:** P-gCN-05 | GCE

$\boldsymbol{I_p}$ (μA) = 0.024 **C** [5-50 μM]; R^2 = 0.963……**:** Bare GCE

The designed sensor's sensitivity to the specific analyte is represented by the slope of the regression equation. By comparing the measured values, it was discovered that the electrode

coated with P-gCN-05 was 7.83 times more sensitive than the bare electrode. For the computation of the limit of detection (LOD), the formula 3σ/b was utilized. In this equation 'b' represents the slope of the regression equation, 'σ' represents the standard deviation of five blank readings. The observational findings showed that the unmodified GCE had a limit of detection (LOD) of 211 nM, while the P-gCN-05 | GCE had a LOD of 7.1 nM. For the purpose of gaining a more comprehensive understanding of the superiority of the newly designed sensor, its performance was evaluated in comparison to that of a number of previously published TRP electrochemical sensors that made use of gCN and other surface modifications of a similar nature.

Table 4.1: A comparison of published electrochemical sensors established for TRP measurement employing gCN, metal oxides, and similar surface modifications with the proposed P-gCN-05 | GCE scaffold.

Electrode Material	***Technique***	***Linear range (µM)***	***LOD (µM)***	***Modification method***	***Ref.***
Co_3O_4/rGO/GCE	LSV	1.0–20, 20–800	0.26	Multistep Synthesis + Drop cast	23
BCN/SPE	DPV	1-400	0.036	Single step Synthesis + Electrodeposition	68
Nanoporous carbon/GCE	Amperometry	1-103	0.03	Single step Synthesis + Drop cast	69
rGO/SnO_2/GCE	DPV	1-100	0.04	Single step Synthesis + Drop cast	70
g-C_3N_4-CPE	LSV	0.1-120	0.085	Single step Synthesis	71
MoS_2/S@gCN/GCE	DPV	0-25	0.03	Multistep Synthesis + Drop cast	72
Ta_2O_5/rGO/GCE	SDLSV	1-800	0.84	Multistep Synthesis + Drop cast	73
Nafion/TiO_2-GR/GCE	DPV	5-140	0.7	Multistep Synthesis + Drop cast	74
MIP/CS/MWCNTs/GCE	DPV	1-300	0.5	Multistep Synthesis + Drop cast	75
P-gCN-05 | GCE	SWV	1-100	0.007	Single step *in*-situ electrodeposition	This work

It is clear from **Table 4.1** that the proposed sensor demonstrated superior characteristics in terms of the ease of creation and its sensitivity. In addition, every single methodology that has been documented in the literature begins with the separate synthesis of distinct ingredients, then moves on to combining and drop-casting the finished product. However, the suggested approach improves its repeatability, practicality, and scalability by allowing for a single-step electrodeposition process with precise control over the layer thickness.

4.3.4 Interference Study

To examine the selectivity and practical utility of the developed sensor for TRP quantification in real samples, its ability to discriminate TRP in presence of other influencing species was tested. To do so, four interferants namely, uric acid (UA), ascorbic acid (AA), dopamine (DA), and hypoxanthine (HX) were chosen because of their presence in human samples and food products. These metabolites might interfere with the TRP electro-oxidation process causing deviations in oxidation peak potential and peak current and thereby challenging the sensor's selectivity. Therefore, the effect of increasing concentration of these interferents on the peak current of 25 µM TRP were investigated. As shown in **Figure 4.9(a)**, all the interfering species exhibited separate peaks and showed no interference with TRP electro-oxidation. Furthermore, no appreciable deviation in the peak current was observed, even when interfering species were present at three times higher concentrations. The results demonstrated the high selectivity of P-gCN-05 | GCE in detecting TRP even in complex mixtures containing potentially identical compounds.

4.3.5 Real Sample Study

To demonstrate the practical applicability of the developed sensor, it was employed to test and validate the TRP in a range of real samples (**Figure 4.9(b-m))**.

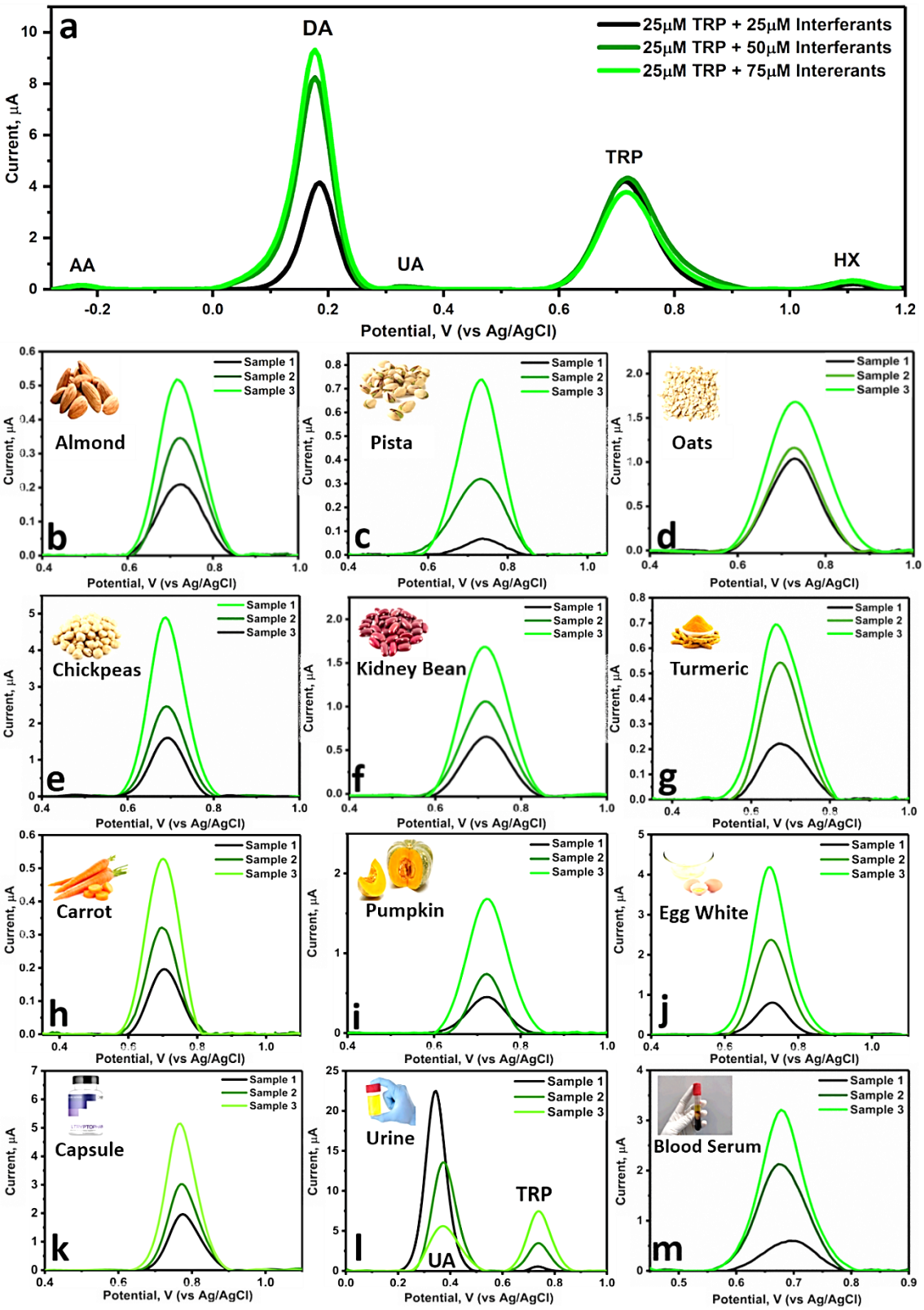

Figure 4.9: Interference Study: (a) Square wave voltammogram using 25 μM of TRP with 1, 2 and 3 times higher concentrations of interferents. Real sample analysis: square wave voltammograms representing the presence of TRP in (b) Almond, (c) Pista, (d) Oats, (e) Chickpea, (f) Kidney beans, (g) Turmeric powder, (h) Carrot, (i) Pumpkin, (j) Egg white, (k) TRP nutritional supplement capsule, (l) Urine, and (m) Blood serum.

Oxin Nutrition L-Tryptophan tablet was chosen as the pharmaceutical sample. Nine different TRP rich food samples were chosen for the real sample analysis: almonds, chickpeas, kidney beans, egg white, pumpkin, carrot, pista, oats, and turmeric powder. Urine sample and blood serum sample of a healthy volunteer was analysed as clinical sample. The individual procedures opted for sample preparation are documented in experimental section. The developed sensor's ability to quantify TRP was next evaluated by recording SWV responses in the prepared test samples. Each sample showed a peak ~ 0.7 V, confirming the presence of tryptophan. To guarantee that the observed peak arises due to electro-oxidation of tryptophan, the samples were spiked with known amount of TRP stock solution. The increase in the peak current on TRP spiking confirmed its association with TRP. The peak current was then utilized to calculate the TRP in the test sample using the previously constructed linear regression equation. **Table 4.2** shows the observed values and the error percentages. The data shows an excellent agreement between the calculated concentrations and the measured values, with a maximum error of 10.0%.

Table 4.2: Quantification of TRP in different real samples using P-gCN-05 | GCE

Real sample	Added (µM)	Found (µM)	% Error
Almond	0	1.11	-
	0.75	1.86	0
	1.5	2.71	6.6
Pista	-	0.42	-
	1	1.48	6
	3	3.72	10
Oats	-	5.47	-
	0.75	6.27	6.6
	3	8.77	10
Chickpea	0	8.56	-
	4	12.92	9
	16	26.01	9

Kidney Beans	0 2 5	3.40 5.58 8.88	- 9 9.6
Turmeric powder	0 1.5 2.5	1.17 2.81 3.67	- 9.3 0
Carrot	0 0.75 1.5	0.79 1.59 2.44	- 6.6 10
Pumpkin	0 1.5 5	2.39 3.88 7.87	- 0 9.6
Egg White	0 5 7.5	4.46 9.94 12.60	- 9.6 8.5
Capsule	10 20 30	10.42 18.29 27.34	4.2 8.5 8.8
Urine	0 15 30	2.92 18.35 35.85	- 2.8 9.7
Human Blood Serum	- 7.5 14	3.13 11.22 17.18	- 7.8 0

4.3.6 Stability, Repeatability and Reproducibility

The P-gCN-05 | GCE's long-term durability was assessed by conducting several cyclic voltammograms in a buffer solution with a pH of 7.4. The voltammograms in **Figure 4.10(a)** indicate that the P-gCN-05 | GCE scaffolds maintained a substantial level of endurance after undergoing a total of 200 CV cycles. Proof that the modified surface will keep its stability throughout time and after repeated use is tested by recording 50 SWV in 0.5 mM $K_3[Fe(CN)_6]$. The peak currents of the first fifty SWV recorded with the single P-gCN-05 | GCE are shown in **Figure 4.10(b)**.

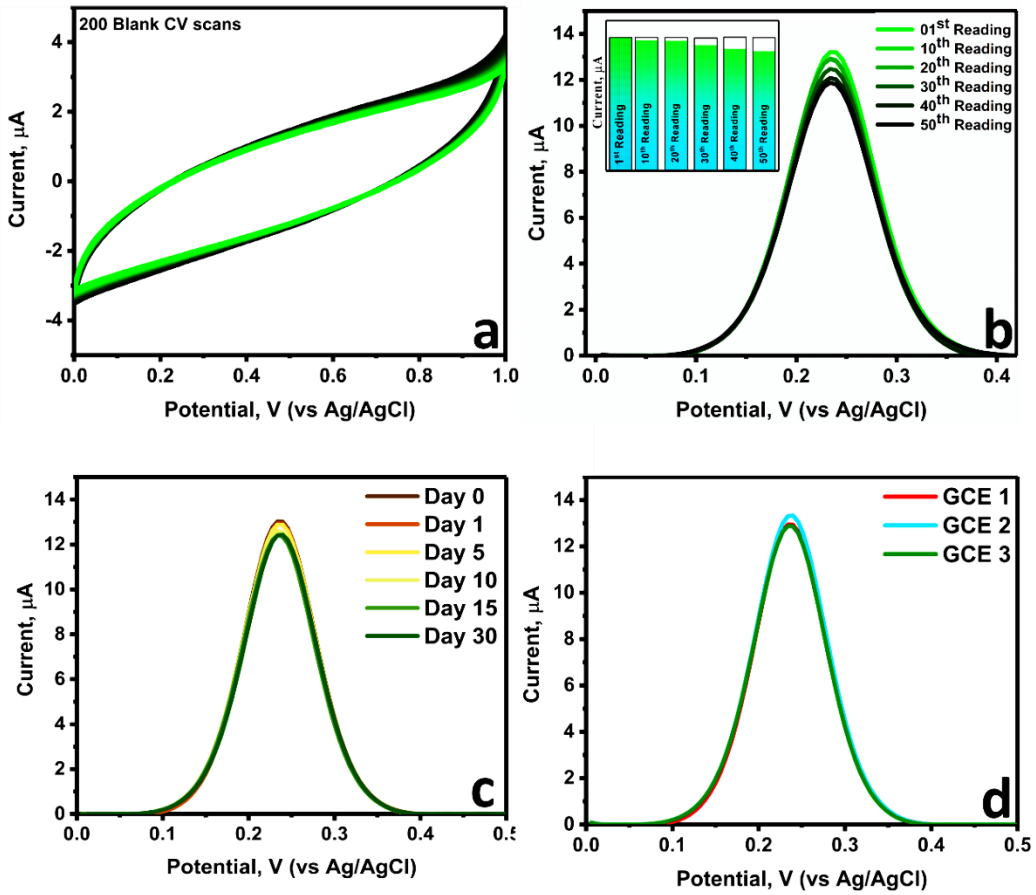

Figure 4.10: (a) 200 consecutive cyclic voltammograms recorded in Phosphate Buffer (PB 7.4) using P-gCN-05 | GCE. (b) First fifty square wave voltammograms as observed for 0.5 mM $K_3[Fe(CN)_6]$ using single P-gCN-05 | GCE. (c) Long term durability current response of 0.5 mM $K_3[Fe(CN)_6]$ for different day using P-gCN-05 | GCE. (d) Square wave voltammograms recorded for 0.5 mM $K_3[Fe(CN)_6]$ using 3 different P-gCN-05 | GCE.

A substantial level of stability was exhibited by the modified GCE, as shown by the bar diagram which displayed a decrease of less than five percent of the original peak current. To investigate the surface's stability and durability over time was tested by recording SWV in 0.5 mM $K_3[Fe(CN)_6]$ for up to 30 days, as shown in **Figure 4.10(c)**. The findings from the SWV indicate that despite the electrodes being stored under typical environmental conditions for a duration of 30 days, only a marginal reduction in peak current was detected. Based on the data, it seems that the scaffold that was created is quite stable and doesn't need any extra storage measures. But keeping the electrodes in a dry place or a nitrogen-filled container will increase their lifespan. To ensure the

reproducibility of the proposed electrodeposition protocol, SWV in 0.5 mM $K_3[Fe(CN)_6]$ were recorded using three different GCE that were modified simultaneously with P-gCN-05. **Figure 4.10(d)** shows the current response of three different electrodes demonstrating excellent reproducibility of the suggested electrodeposition procedure.

4.4. Conclusions

This work presents the synthesis and electrodeposition of graphitic carbon nitride doped with P. With the intricate mechanistic understanding of electrodeposition, new insights into the composition, topography, and electrochemistry of the electrodeposited P-gCN are provided. Electrodeposition method showed superior electrochemical performance compared to drop-coating method, exhibiting 7.5 times higher current and ~ 0.10 V negative potential shift for TRP electro-oxidation, indicating remarkable electrocatalytic activity. Showcasing a detection limit of 7.1 nM, the P-gCN | GCE manifested its excellent sensitivity. The selectivity of the sensor was ensured from its unaltered peak potential and peak current, even when numerous possible interferents, such as ascorbic acid, uric acid, dopamine, and hypoxanthine, were present in high concentrations. More than ten real samples, including food products like eggs, pumpkins, carrots, and almonds as well as nutritional supplements and human urine, blood samples, were successfully quantified for TRP using the developed P-gCN-05 | GCE. The real sample analysis highlights the real life utility of the proposed sensor for keeping a check on TRP levels in the food and pharmaceutical industries as well as for clinical diagnosis. Furthermore, the developed sensor demonstrated excellent stability exhibiting less than 5 % of decrease in peak current even after 30 days. It was discovered that the suggested electrodeposition protocol exhibited notable reproducibility and repeatability over both the same and different glassy carbon electrodes, suggesting the electrodeposition strategy's potential to produce a reliable and controlled surface modification.

4.5. References:

(1) Dalgliesh, C. E. Biological Degradation of Tryptophan. *Q. Rev. Chem. Soc.* **1951**, *5* (3), 227–244. https://doi.org/10.1039/QR9510500227.

(2) Le Floc'h, N.; Otten, W.; Merlot, E. Tryptophan Metabolism, from Nutrition to Potential Therapeutic Applications. *Amino Acids* **2011**, *41* (5), 1195–1205. https://doi.org/10.1007/s00726-010-0752-7.

(3) Zhang, J.; Huang, Y.; Yue, D.; Cui, Y.; Yang, Y.; Qian, G. A Luminescent Turn-up Metal-Organic Framework Sensor for Tryptophan Based on Singlet-Singlet Förster Energy Transfer. *J. Mater. Chem. B* **2018**, *6* (31), 5174–5180. https://doi.org/10.1039/c8tb01592a.

(4) Wu, B.; Xiao, L.; Zhang, M.; Yang, C.; Li, Q.; Li, G.; He, Q.; Liu, J. Facile Synthesis of Dendritic-like CeO2/RGO Composite and Application for Detection of Uric Acid and Tryptophan Simultaneously. *J. Solid State Chem.* **2021**, *296*, 122023. https://doi.org/10.1016/J.JSSC.2021.122023.

(5) Xia, Y.; Zhao, F.; Zeng, B. A Molecularly Imprinted Copolymer Based Electrochemical Sensor for the Highly Sensitive Detection of L-Tryptophan. *Talanta* **2020**, *206*, 120245. https://doi.org/10.1016/J.TALANTA.2019.120245.

(6) Wang, L.; Yang, R.; Li, J.; Qu, L.; Harrington, P. de B. A Highly Selective and Sensitive Electrochemical Sensor for Tryptophan Based on the Excellent Surface Adsorption and Electrochemical Properties of PSS Functionalized Graphene. *Talanta* **2019**, *196*, 309–316. https://doi.org/10.1016/J.TALANTA.2018.12.058.

(7) Millward, D. J. Identifying Recommended Dietary Allowances for Protein and Amino Acids: A Critique of the 2007 WHO/FAO/UNU Report. *Br. J. Nutr.* **2012**, *108* (SUPPL. 2). https://doi.org/10.1017/S0007114512002450.

(8) Sutanto, C. N.; Loh, W. W.; Kim, J. E. The Impact of Tryptophan Supplementation

on Sleep Quality: A Systematic Review, Meta-Analysis, and Meta-Regression. *Nutr. Rev.* **2022**, *80* (2), 306–316. https://doi.org/10.1093/nutrit/nuab027.

(9) Kokturk, O.; Kanbay, A. Tryptophan Metabolism and Sleep. In *Molecular and Integrative Toxicology*; Springer Science+Business Media B.V., 2015; pp 239–252. https://doi.org/10.1007/978-3-319-15630-9_10.

(10) Strasser, B.; Gostner, J. M.; Fuchs, D. Mood, Food, and Cognition: Role of Tryptophan and Serotonin. *Curr. Opin. Clin. Nutr. Metab. Care* **2016**, *19* (1), 55–61. https://doi.org/10.1097/MCO.0000000000000237.

(11) Zhang, Y.; Waterhouse, G. I. N.; Xiang, Z. peng; Che, J.; Chen, C.; Sun, W. A Highly Sensitive Electrochemical Sensor Containing Nitrogen-Doped Ordered Mesoporous Carbon (NOMC) for Voltammetric Determination of l-Tryptophan. *Food Chem.* **2020**, *326*, 126976. https://doi.org/10.1016/J.FOODCHEM.2020.126976.

(12) Prabhu, P.; Babu, R. S.; Narayanan, S. S. Electrocatalytic Oxidation of L-Tryptophan Using Copper Hexacyanoferrate Film Modified Gold Nanoparticle Graphite-Wax Electrode. *Colloids Surfaces B Biointerfaces* **2011**, *87* (1), 103–108. https://doi.org/10.1016/J.COLSURFB.2011.05.008.

(13) van der Goot, A. T.; Zhu, W.; Vázquez-Manrique, R. P.; Seinstra, R. I.; Dettmer, K.; Michels, H.; Farina, F.; Krijnen, J.; Melki, R.; Buijsman, R. C.; Ruiz Silva, M.; Thijssen, K. L.; Kema, I. P.; Neri, C.; Oefner, P. J.; Nollen, E. A. A. Delaying Aging and the Aging-Associated Decline in Protein Homeostasis by Inhibition of Tryptophan Degradation. *Proc. Natl. Acad. Sci. U. S. A.* **2012**, *109* (37), 14912–14917. https://doi.org/10.1073/pnas.1203083109.

(14) Hertzman, P. A.; Blevins, W. L.; Mayer, J.; Greenfield, B.; Ting, M.; Gleich, G. J. Association of the Eosinophilia–Myalgia Syndrome with the Ingestion of

Tryptophan. *http://dx.doi.org/10.1056/NEJM199003293221301* **2010**, *322* (13), 869–873. https://doi.org/10.1056/NEJM199003293221301.

(15) Zádor, F.; Nagy-Grócz, G.; Kekesi, G.; Dvorácskó, S.; Szucs, E.; Tömböly, C.; Horvath, G.; Benyhe, S.; Vécsei, L. Kynurenines and the Endocannabinoid System in Schizophrenia: Common Points and Potential Interactions. *Molecules* **2019**, *24* (20). https://doi.org/10.3390/MOLECULES24203709.

(16) Çevikkalp, S. A.; Löker, G. B.; Yaman, M.; Amoutzopoulos, B. A Simplified HPLC Method for Determination of Tryptophan in Some Cereals and Legumes. *Food Chem.* **2016**, *193*, 26–29. https://doi.org/10.1016/j.foodchem.2015.02.108.

(17) Danielson, N. D.; Rogers, L. B. Determination of Tryptophan in Proteins by Pyrolysis Gas Chromatography. *Anal. Chem.* **1978**, *50* (12), 1680–1683. https://doi.org/10.1021/ac50034a027.

(18) Kato, N.; Kojima, T.; Yoshiyagawa, S.; Ohta, H.; Toriba, A.; Nishimura, H.; Hayakawa, K. Rapid and Sensitive Determination of Tryptophan, Serotonin and Psychoactive Tryptamines by Thin-Layer Chromatography/Fluorescence Detection. *J. Chromatogr. A* **2007**, *1145* (1–2), 229–233. https://doi.org/10.1016/j.chroma.2007.01.061.

(19) Ravindran, G.; Bryden, W. L. Tryptophan Determination in Proteins and Feedstuffs by Ion Exchange Chromatography. *Food Chem.* **2005**, *89* (2), 309–314. https://doi.org/10.1016/j.foodchem.2004.05.035.

(20) Wu, Y.; Wang, T.; Zhang, C.; Xing, X.-H. A Rapid and Specific Colorimetric Method for Free Tryptophan Quantification. *Talanta* **2018**, *176*, 604–609. https://doi.org/10.1016/j.talanta.2017.08.002.

(21) Li, J.; Du, N.; Guan, R.; Zhao, S. Construction of a Chiral Fluorescent Probe for Tryptophan Enantiomers/Ascorbic Acid Identification. *ACS Appl. Mater.*

Interfaces **2023**, *15* (19), 23642–23652. https://doi.org/10.1021/acsami.3c02423.

(22) Altria, K. D.; Harkin, P.; Hindson, M. G. Quantitative Determination of Tryptophan Enantiomers by Capillary Electrophoresis. *J. Chromatogr. B. Biomed. Appl.* **1996**, *686* (1), 103–110. https://doi.org/10.1016/s0378-4347(96)00037-0.

(23) Zhang, S.; Ling, P.; Chen, Y.; Liu, J.; Yang, C. 2D/2D Porous Co3O4/RGO Nanosheets Act as an Electrochemical Sensor for Voltammetric Tryptophan Detection. *Diam. Relat. Mater.* **2023**, *135*, 109811. https://doi.org/10.1016/j.diamond.2023.109811.

(24) Kesavan, G.; Chen, S. M. Highly Sensitive Electrochemical Sensor Based on Carbon-Rich Graphitic Carbon Nitride as an Electrocatalyst for the Detection of Diphenylamine. *Microchem. J.* **2020**, *159* (October), 105587. https://doi.org/10.1016/j.microc.2020.105587.

(25) Kumar Singh, A.; Das, C.; Indra, A. Scope and Prospect of Transition Metal-Based Cocatalysts for Visible Light-Driven Photocatalytic Hydrogen Evolution with Graphitic Carbon Nitride. *Coord. Chem. Rev.* **2022**, *465*, 214516. https://doi.org/10.1016/J.CCR.2022.214516.

(26) Lv, J.; Li, C.; Feng, S.; Chen, S. M.; Ding, Y.; Chen, C.; Hao, Q.; Yang, T. H.; Lei, W. A Novel Electrochemical Sensor for Uric Acid Detection Based on PCN/MWCNT. *Ionics (Kiel).* **2019**, *25* (9), 4437–4445. https://doi.org/10.1007/s11581-019-03010-8.

(27) Jiang, L.; Yuan, X.; Pan, Y.; Liang, J.; Zeng, G.; Wu, Z.; Wang, H. Doping of Graphitic Carbon Nitride for Photocatalysis: A Review. *Appl. Catal. B Environ.* **2017**, *217*, 388–406. https://doi.org/10.1016/J.APCATB.2017.06.003.

(28) Sagara, N.; Kamimura, S.; Tsubota, T.; Ohno, T. Photoelectrochemical CO2 Reduction by a P-Type Boron-Doped g-C3N4 Electrode under Visible Light. *Appl.*

Catal. B Environ. **2016**, *192*, 193–198. https://doi.org/10.1016/j.apcatb.2016.03.055.

(29) Chen, Z.; Fan, T.-T.; Yu, X.; Wu, Q.-L.; Zhu, Q.-H.; Zhang, L.-Z.; Li, J.-H.; Fang, W.-P.; Yi, X.-D. Gradual Carbon Doping of Graphitic Carbon Nitride towards Metal-Free Visible Light Photocatalytic Hydrogen Evolution. *J. Mater. Chem. A* **2018**, *6* (31), 15310–15319. https://doi.org/10.1039/C8TA03303J.

(30) Fang, J.; Fan, H.; Li, M.; Long, C. Nitrogen Self-Doped Graphitic Carbon Nitride as Efficient Visible Light Photocatalyst for Hydrogen Evolution. *J. Mater. Chem. A* **2015**, *3* (26), 13819–13826. https://doi.org/10.1039/C5TA02257F.

(31) Huang, Z.-F.; Song, J.; Pan, L.; Wang, Z.; Zhang, X.; Zou, J.-J.; Mi, W.; Zhang, X.; Wang, L. Carbon Nitride with Simultaneous Porous Network and O-Doping for Efficient Solar-Energy-Driven Hydrogen Evolution. *Nano Energy* **2015**, *12*, 646–656. https://doi.org/10.1016/j.nanoen.2015.01.043.

(32) Zhou, Y.; Zhang, L.; Liu, J.; Fan, X.; Wang, B.; Wang, M.; Ren, W.; Wang, J.; Li, M.; Shi, J. Brand New P-Doped g-C 3 N 4 : Enhanced Photocatalytic Activity for H 2 Evolution and Rhodamine B Degradation under Visible Light. *J. Mater. Chem. A* **2015**, *3* (7), 3862–3867. https://doi.org/10.1039/C4TA05292G.

(33) Wang, Y.; Di, Y.; Antonietti, M.; Li, H.; Chen, X.; Wang, X. Excellent Visible-Light Photocatalysis of Fluorinated Polymeric Carbon Nitride Solids. *Chem. Mater.* **2010**, *22* (18), 5119–5121. https://doi.org/10.1021/cm1019102.

(34) Mohammad, A.; Chandra, P.; Khan, M. E.; Choi, C. H.; Yoon, T. Sulfur-Doped Graphitic Carbon Nitride: Tailored Nanostructures for Photocatalytic, Sensing, and Energy Storage Applications. *Adv. Colloid Interface Sci.* **2023**, *322*, 103048. https://doi.org/10.1016/J.CIS.2023.103048.

(35) Ou, H.; Tang, C.; Zhang, Y.; Asiri, A. M.; Titirici, M. M.; Wang, X. Se-Modified

Polymeric Carbon Nitride Nanosheets with Improved Photocatalytic Activities. *J. Catal.* **2019**, *375*, 104–112. https://doi.org/10.1016/J.JCAT.2019.05.029.

(36) Fina, F.; Callear, S. K.; Carins, G. M.; Irvine, J. T. S. Structural Investigation of Graphitic Carbon Nitride via XRD and Neutron Diffraction. *Chem. Mater.* **2015**, *27* (7), 2612–2618. https://doi.org/10.1021/acs.chemmater.5b00411.

(37) Li, X.; Zhang, J.; Shen, L.; Ma, Y.; Lei, W.; Cui, Q.; Zou, G. Preparation and Characterization of Graphitic Carbon Nitride through Pyrolysis of Melamine. *Appl. Phys. A Mater. Sci. Process.* **2009**, *94* (2), 387–392. https://doi.org/10.1007/S00339-008-4816-4.

(38) Liu, L.-L.; Chen, F.; Wu, J.-H.; Li, W.-W.; Chen, J.-J.; Yu, H.-Q. Fine Tuning of Phosphorus Active Sites on G-C 3 N 4 Nanosheets for Enhanced Photocatalytic Decontamination. *J. Mater. Chem. A* **2021**, *9* (17), 10933–10944. https://doi.org/10.1039/D1TA01537K.

(39) Choudhary, P.; Kumar, A.; Krishnan, V. Nanoarchitectonics of Phosphorylated Graphitic Carbon Nitride for Sustainable, Selective and Metal-Free Synthesis of Primary Amides. *Chem. Eng. J.* **2022**, *431*, 133695. https://doi.org/10.1016/j.cej.2021.133695.

(40) Lan, Z.-Y.; Vasu, D.; Liu, Y.-C.; You, Y.-F.; Chiu, T.-W.; Chen, P. C. Oxygen-Phosphorus-Codoped Graphitic Carbon Nitride Nanosheets with Better Photocatalytic Ability towards the Degradation of Rhodamine-B Dyes. *New J. Chem.* **2023**, *47* (28), 13117–13126. https://doi.org/10.1039/D3NJ02083E.

(41) Kesavan, G.; Vinothkumar, V.; Chen, S. M.; Thangadurai, D. T. Phosphorus-Doped Graphitic Carbon Nitride: A Metal-Free Electrocatalyst for Quercetin Sensing in Fruit Samples. *Electrochim. Acta* **2022**, *426*, 140759. https://doi.org/10.1016/J.ELECTACTA.2022.140759.

(42) Ran, J.; Ma, T. Y.; Gao, G.; Du, X. W.; Qiao, S. Z. Porous P-Doped Graphitic Carbon Nitride Nanosheets for Synergistically Enhanced Visible-Light Photocatalytic H2 Production. *Energy Environ. Sci.* **2015**, *8* (12), 3708–3717. https://doi.org/10.1039/C5EE02650D.

(43) Zhang, C.; Liu, J.; Huang, X.; Chen, D.; Xu, S. Multistage Polymerization Design for G-C 3 N 4 Nanosheets with Enhanced Photocatalytic Activity by Modifying the Polymerization Process of Melamine. *ACS Omega* **2019**, *4* (17), 17148–17159. https://doi.org/10.1021/acsomega.9b01510.

(44) Sunasee, S.; Leong, K. H.; Wong, K. T.; Lee, G.; Pichiah, S.; Nah, I.; Jeon, B.-H.; Yoon, Y.; Jang, M. Sonophotocatalytic Degradation of Bisphenol A and Its Intermediates with Graphitic Carbon Nitride. *Environ. Sci. Pollut. Res. Int.* **2019**, *26* (2), 1082–1093. https://doi.org/10.1007/s11356-017-8729-7.

(45) Chen, Y.; Qu, Y.; Xu, P.; Zhou, X.; Sun, J. Insight into the Influence of Donor-Acceptor System on Graphitic Carbon Nitride Nanosheets for Transport of Photoinduced Charge Carriers and Photocatalytic H2 Generation. *J. Colloid Interface Sci.* **2021**, *601*, 326–337. https://doi.org/10.1016/j.jcis.2021.05.145.

(46) Zhang, Y.; Mori, T.; Ye, J.; Antonietti, M. Phosphorus-Doped Carbon Nitride Solid: Enhanced Electrical Conductivity and Photocurrent Generation. *J. Am. Chem. Soc.* **2010**, *132* (18), 6294–6295. https://doi.org/10.1021/ja101749y.

(47) Ma, T. Y.; Ran, J.; Dai, S.; Jaroniec, M.; Qiao, S. Z. Phosphorus-Doped Graphitic Carbon Nitrides Grown In Situ on Carbon-Fiber Paper: Flexible and Reversible Oxygen Electrodes. *Angew. Chemie* **2015**, *127* (15), 4729–4733. https://doi.org/10.1002/ANGE.201411125.

(48) Zhu, Y.; Li, J.; Cao, J.; Lv, C.; Huang, G.; Zhang, G.; Xu, Y.; Zhang, S.; Meng, P.; Zhan, T.; Yang, D. Phosphorus-Doped Polymeric Carbon Nitride Nanosheets

for Enhanced Photocatalytic Hydrogen Production. *APL Mater.* **2020**, *8* (4). https://doi.org/10.1063/1.5143711/1064604.

(49) Hellgren, N.; Haasch, R. T.; Schmidt, S.; Hultman, L.; Petrov, I. Interpretation of X-Ray Photoelectron Spectra of Carbon-Nitride Thin Films: New Insights from in Situ XPS. *Carbon N. Y.* **2016**, *108*, 242–252. https://doi.org/10.1016/J.CARBON.2016.07.017.

(50) You, S.; Guo, S.; Zhao, X.; Sun, M.; Sun, C.; Su, Z.; Wang, X. All-Inorganic Perovskite/Graphitic Carbon Nitride Composites for CO 2 Photoreduction into C1 Compounds under Low Concentrations of CO 2. *Dalt. Trans.* **2019**, *48* (37), 14115–14121. https://doi.org/10.1039/C9DT02468A.

(51) Li, C.; Yang, X.; Yang, B.; Yan, Y.; Qian, Y. Synthesis and Characterization of Nitrogen-Rich Graphitic Carbon Nitride. *Mater. Chem. Phys.* **2007**, *103* (2–3), 427–432. https://doi.org/10.1016/J.MATCHEMPHYS.2007.02.057.

(52) Hoh, H. Y.; Zhang, Y.; Lin Zhong, Y.; Bao, Q.; Hoh, H. Y.; Zhang, Y.; Zhong, Y. L.; Bao, Q. Harnessing the Potential of Graphitic Carbon Nitride for Optoelectronic Applications. *Adv. Opt. Mater.* **2021**, *9* (16), 2100146. https://doi.org/10.1002/ADOM.202100146.

(53) Li, X.; Zhang, J.; Shen, L.; Ma, Y.; Lei, W.; Cui, Q.; Zou, G. Preparation and Characterization of Graphitic Carbon Nitride through Pyrolysis of Melamine. *Appl. Phys. A Mater. Sci. Process.* **2009**, *94* (2), 387–392. https://doi.org/10.1007/S00339-008-4816-4.

(54) Li, K.; Yan, L.; Zeng, Z.; Luo, S.; Luo, X.; Liu, X.; Guo, H.; Guo, Y. Fabrication of H3PW12O40-Doped Carbon Nitride Nanotubes by One-Step Hydrothermal Treatment Strategy and Their Efficient Visible-Light Photocatalytic Activity toward Representative Aqueous Persistent Organic Pollutants Degradation. *Appl.*

Catal. B Environ. **2014**, *156–157*, 141–152. https://doi.org/10.1016/J.APCATB.2014.03.010.

(55) Majumdar, A.; Das, S. C.; Shripathi, T.; Heinicke, J.; Hippler, R. Shake up Satellites and Fluorescence Property of Carbon Nitride and Hydrogenated Carbon Nitride: Annealing Effect. *Surf. Sci.* **2013**, *609*, 53–61. https://doi.org/10.1016/J.SUSC.2012.11.003.

(56) Alwin, E.; Nowicki, W.; Wojcieszak, R.; Zieliński, M.; Pietrowski, M. Elucidating the Structure of the Graphitic Carbon Nitride Nanomaterials via X-Ray Photoelectron Spectroscopy and X-Ray Powder Diffraction Techniques. *Dalt. Trans.* **2020**, *49* (36), 12805–12813. https://doi.org/10.1039/D0DT02325F.

(57) Gengenbach, T. R.; Major, G. H.; Linford, M. R.; Easton, C. D. Practical Guides for X-Ray Photoelectron Spectroscopy (XPS): Interpreting the Carbon 1s Spectrum. *J. Vac. Sci. Technol. A Vacuum, Surfaces, Film.* **2021**, *39* (1), 13204. https://doi.org/10.1116/6.0000682/246569.

(58) Yang, F.; Lublow, M.; Orthmann, S.; Merschjann, C.; Tyborski, T.; Rusu, M.; Kubala, S.; Thomas, A.; Arrigo, R.; Hävecker, M.; Schedel-Niedrig, T. Metal-Free Photocatalytic Graphitic Carbon Nitride on p-Type Chalcopyrite as a Composite Photocathode for Light-Induced Hydrogen Evolution. *ChemSusChem* **2012**, *5* (7), 1227–1232. https://doi.org/10.1002/CSSC.201100691.

(59) Liu, Y.; Zhao, S.; Zhang, C.; Fang, J.; Xie, L.; Zhou, Y.; Zhuo, S. Hollow Tubular Carbon Doping Graphitic Carbon Nitride with Adjustable Structure for Highly Enhanced Photocatalytic Hydrogen Production. *Carbon N. Y.* **2021**, *182*, 287–296. https://doi.org/10.1016/J.CARBON.2021.06.008.

(60) Titantah, J. T.; Lamoen, D. Carbon and Nitrogen 1s Energy Levels in Amorphous Carbon Nitride Systems: XPS Interpretation Using First-Principles. *Diam. Relat.*

Mater. **2007**, *16* (3), 581–588. https://doi.org/10.1016/J.DIAMOND.2006.11.048.

(61) Kaliyaraj Selva Kumar, A.; Zhang, Y.; Li, D.; Compton, R. G. A Mini-Review: How Reliable Is the Drop Casting Technique? *Electrochem. commun.* **2020**, *121*, 106867. https://doi.org/10.1016/J.ELECOM.2020.106867.

(62) Singh, A. K.; Keshari, P.; Saroj, A.; Ramanathan, V.; Rosy. Electrodeposition of Graphitic Carbon Nitride and Its In Situ Decoration with MnO2 Nanostructures: A Tailored Interface for Dopamine Sensing. *Surfaces and Interfaces* **2023**, *42*, 103316. https://doi.org/10.1016/j.surfin.2023.103316.

(63) Baskar, S.; Liao, C. W.; Chang, J. L.; Zen, J. M. Electrochemical Synthesis of Electroactive Poly(Melamine) with Mechanistic Explanation and Its Applicability to Functionalize Carbon Surface to Prepare Nanotube-Nanoparticles Hybrid. *Electrochim. Acta* **2013**, *88*, 1–5. https://doi.org/10.1016/j.electacta.2012.10.040.

(64) Alwin, E.; Nowicki, W.; Wojcieszak, R.; Zieliński, M.; Pietrowski, M. Elucidating the Structure of the Graphitic Carbon Nitride Nanomaterials via X-Ray Photoelectron Spectroscopy and X-Ray Powder Diffraction Techniques. *Dalt. Trans.* **2020**, *49* (36), 12805–12813. https://doi.org/10.1039/D0DT02325F.

(65) Guo, S.; Deng, Z.; Li, M.; Jiang, B.; Tian, C.; Pan, Q.; Fu, H. Phosphorus-Doped Carbon Nitride Tubes with a Layered Micro-nanostructure for Enhanced Visible-Light Photocatalytic Hydrogen Evolution. *Angew. Chemie Int. Ed.* **2016**, *55* (5), 1830–1834. https://doi.org/10.1002/anie.201508505.

(66) Ju, E.; Dong, K.; Chen, Z.; Liu, Z.; Liu, C.; Huang, Y.; Wang, Z.; Pu, F.; Ren, J.; Qu, X. Copper(II)–Graphitic Carbon Nitride Triggered Synergy: Improved ROS Generation and Reduced Glutathione Levels for Enhanced Photodynamic Therapy. *Angew. Chemie Int. Ed.* **2016**, *55* (38), 11467–11471. https://doi.org/10.1002/anie.201605509.

(67) Yadav, K.; Garg, S.; Singh, A. K.; Singh, S.; Singh Parmar, A.; Rosy. Protein Nano Dots Conjugated AuNP, Poly-Lysine Biointerface for the Selective Voltammetric Estimation of Melatonin in Pharmaceutical and Food Samples. *Microchem. J.* **2022**, *179*, 107563. https://doi.org/10.1016/j.microc.2022.107563.

(68) Garg, S.; Singh, A.; Parmar, A. S.; Rosy, N. Boron Carbon Nitride-Assisted Electro-Functionalization of Screen-Printed Electrode for Tryptophan Sensing. *ACS Appl. Nano Mater.* **2023**, *7*, 2023. https://doi.org/10.1021/acsanm.3c02396.

(69) Han, J.; Zhao, J.; Li, Z.; Zhang, H.; Yan, Y.; Cao, D.; Wang, G. Nanoporous Carbon Derived from Dandelion Pappus as an Enhanced Electrode Material with Low Cost for Amperometric Detection of Tryptophan. *J. Electroanal. Chem.* **2018**, *818*, 149–156. https://doi.org/10.1016/j.jelechem.2018.04.044.

(70) Li, Y.-J.; Yang, L.-L.; Ni, L.; Xiong, J.-M.; He, J.-Y.; Zhou, L.-D.; Luo, L.; Zhang, Q.-H.; Yuan, C.-S. Constructing Electrochemical Sensor Using Molecular-Imprinted Polysaccharide for Rapid Identification and Determination of l-Tryptophan in Diet. *Food Chem.* **2023**, *425*, 136486. https://doi.org/10.1016/j.foodchem.2023.136486.

(71) Abebe, H. A.; Diro, A.; Kitte, S. A. Voltammetric Determination of Tryptophan at Graphitic Carbon Nitride Modified Carbon Paste Electrode. *Heliyon* **2023**, *9* (10), e21033. https://doi.org/10.1016/j.heliyon.2023.e21033.

(72) Niyitanga, T.; Pathak, A.; Chaudhary, A.; Khan, R. A.; Kim, H. MoS2/S@gCN Composite Electrode for L-Tryptophan Sensing. *Biosensors* **2023**, *13* (11), 967. https://doi.org/10.3390/bios13110967.

(73) Zhou, S.; Deng, Z.; Wu, Z.; Xie, M.; Tian, Y.; Wu, Y.; Liu, J.; Li, G.; He, Q. Ta2O5/RGO Nanocomposite Modified Electrodes for Detection of Tryptophan through Electrochemical Route. *Nanomaterials* **2019**, *9* (6), 811.

https://doi.org/10.3390/nano9060811.

(74) Fan, Y.; Liu, J.-H.; Lu, H.-T.; Zhang, Q. Electrochemistry and Voltammetric Determination of L-Tryptophan and L-Tyrosine Using a Glassy Carbon Electrode Modified with a Nafion/TiO2-Graphene Composite Film. *Microchim. Acta* **2011**, *173* (1–2), 241–247. https://doi.org/10.1007/s00604-011-0556-9.

(75) Li, Y.-J.; Yang, L.-L.; Ni, L.; Xiong, J.-M.; He, J.-Y.; Zhou, L.-D.; Luo, L.; Zhang, Q.-H.; Yuan, C.-S. Constructing Electrochemical Sensor Using Molecular-Imprinted Polysaccharide for Rapid Identification and Determination of l-Tryptophan in Diet. *Food Chem.* **2023**, *425*, 136486. https://doi.org/10.1016/j.foodchem.2023.136486.